Supplementary Information for 'Molecular Dynamics Simulation of Potentiometric Sensor Response: Effect of Biomolecules, Surface Morphology and Surface Charge'

B. M. Lowe, C-K. Skylaris, N. G. Green, Y. Shibuta and T. Sakata

Table of Contents

1 Electrical Double Layer Analytical Modelling

In this section a more detailed background for common mean-field/analytical models of the Electrical Double Layer is presented. At the following URL we also provide visualisations of the surface potential shift due to binding of molecules as described by Equation 5 from the main text for the Poisson-Boltzmann Equation (both monovalent and mixed valency), the Debye-Hückel Equation and the modified Poisson-Boltzmann equation. The open-source Python code is also provided to allow researchers to explore these equations:

`https://github.com/bml1g12/P-B-SurfPot-Calc/blob/master/SurfaceChargeCalculations.ipynb`

At the time of writing, this code can also be run interactively in a web-browser from the following URL:

`https://mybinder.org/v2/gh/bml1g12/P-B-SurfPot-Calc/master?filepath=SurfaceChargeCalculations.ipynb`

1.1 Helmholtz-Perrin Model

The simplest and most common model of BioFET response treat the response due to biomolecules as charge on a parallel plate capacitor model of the surface (also called the 'constant capacitance' model or Helmholtz-Perrin model[1]). In such models, the measured change in potential is assumed to be equal to the change in surface charge from biomolecule binding, divided by a capacitance value which describes the coupling of the analyte to the FET semiconducting channel[2,3]. This capacitance is often measured for the specific system in question[3,4] or estimated within a broad range based on physical considerations[5]. This model neglects an explicit description of the effect of electrolyte ionic strength and is the most commonly used empirical model for estimating the charge induced in the channel due to binding of biomolecules from a measured change in potential.

1.2 Poisson-Boltzmann Equation and Grahame Equation

The Poisson-Boltzmann equation treats the ions as point charges in thermal equilibrium in the presence of a uniformly charged surface and only considers Coulombic interactions[6,7]:

$$\nabla^2\phi_{\mathrm{pb}}(r) = -\frac{q}{\varepsilon_0\varepsilon_{\mathrm{r}}}\sum_i z_i c_{i\infty}\exp\left(\frac{-qz_i\phi_{\mathrm{pb}}(r)}{k_{\mathrm{b}}T}\right), \tag{1}$$

where $\phi(r)$ is the electric potential as a function of distance r, q is the elementary charge, ε_0 is the permittivity of free space, ε_{r} is the relative permittivity of the medium, z_i is the valence of the electrolyte ion i, $c_{i\infty}$ is the bulk concentration of electrolyte ion i (expressed as a number density), k_{b} is the Boltzmann constant and T is the temperature.

By considering the total charge per unit area within the electrical double layer (q_{edl}) and charge-neutrality, one can obtain the surface charge, $\sigma = -q_{\mathrm{edl}}$, as a function of surface potential[8]. When obtained from the Poisson-Boltzmann (Equation 1), the surface charge-potential relation is often termed the Grahame equation[8]:

$$\sigma_{\mathrm{pb}} = \sqrt{8k_{\mathrm{b}}T\varepsilon_0\varepsilon_{\mathrm{r}}c_\infty}\sinh\left(\frac{qz\phi_{\mathrm{s}}}{2k_{\mathrm{b}}T}\right), \tag{2}$$

where ϕ_{s} is the surface potential (i.e. potential difference between surface and the bulk electrolyte).

1.3 Linearised Poisson-Boltzmann Equation and Debye-Hückel model

Assuming ϕ is small ($|\frac{qz_i\phi(r)}{k_{\mathrm{b}}T}| \ll 1$) the Poisson-Boltzmann equation can be linearised resulting in Equation 3[6,7,9,10]:

$$\nabla^2\phi_{\mathrm{dh}}(r) = \left[\frac{1}{\varepsilon_0\varepsilon_{\mathrm{r}}}\sum_i \frac{q^2z_i^2c_{i\infty}}{k_{\mathrm{b}}T}\right]\phi_{\mathrm{dh}}(r) = \kappa^2\phi_{\mathrm{dh}}(r), \tag{3}$$

in which κ^{-1} is the Debye length. The approximation of assuming ϕ is small is termed the Debye-Hückel approximation, which has an analytical solution:

$$\phi_{\mathrm{dh}}(r) = \phi_{\mathrm{s}}\exp(-\kappa r), \tag{4}$$

Despite this approximation not being strictly valid in most situations of interest in colloid science and electrochemistry[6], it is commonly used. One reason for this is its convenience, whereby electrostatic screening by electrolyte can be described in a simple parameter - the Debye length, which is inversely proportional to the square root of the ionic strength. From the linearised Poisson-Boltzmann equation (Equation 3), similarly to before (Equation 2), the surface charge density can be obtained as a function of potential (Equation 1.26 of reference[8]):

$$\sigma_{\mathrm{dh}} = \phi_s\varepsilon_0\varepsilon_{\mathrm{r}}\kappa \tag{5}$$

The Poisson-Boltzmann equation neglects finite size effects, and thus provides inaccurate results for highly concentrated systems. One way of dealing with this is the incorporation of a parallel plate-like layer at the surface which represents accumulated charge, called the Stern layer. By combining the Stern layer with Equation 4 for a surface system, the commonly used Gouy-Chapmann-Stern electrical double layer model is constructed.

1.4 Modified Poisson-Boltzmann Equation

An alternative method which does not require empirical fitting of the Stern layer capacitance is the 'modified' Poisson-Boltzmann equation, as shown in Equation 6 for a z:z symmetric electrolyte[11]. The modified Poisson-Boltzmann equation simply constrains the maximum density of counterions permissible at the surface to an (semi-)empirical finite value based on packing constraints:

$$\Delta^2\phi_{\mathrm{mpb}} = \frac{zqc_{i\infty}}{\varepsilon_0\varepsilon_{\mathrm{r}}}\frac{2\sinh(2q\phi_{\mathrm{mpb}}/(k_{\mathrm{b}}T))}{1+2v\sinh^2(zq\phi_{\mathrm{mpb}}/(2k_{\mathrm{b}}T))}, \tag{6}$$

where $v = 2a^3c_\infty$ is a dimensionless measure of the non-diluteness by which a represents the mean spacing of ions at their maximum possible concentration ($a = c_{\mathrm{max}}^{-1/3}$) .[11,12] From the modified Poisson-Boltzmann equation (Equation 6), similarly to before with the Grahame equation, the relationship between the surface charge and the potential can be obtained (Equation 28 of reference[11]):

$$\sigma_{\mathrm{mpb}} = \mathrm{sgn}(\phi_{\mathrm{s}})2zqc_{i\infty}\kappa^{-1}\sqrt{\frac{2}{v}\ln\left[1+2v\sinh^2\left(\frac{zq\phi_{\mathrm{s}}}{2k_{\mathrm{b}}T}\right)\right]} \tag{7}$$

In the main paper, the surface charge to surface potential relationship was discussed, an important metric for which is differential capacitance is:

$$C_D = \frac{-dq_{\mathrm{edl}}}{d\phi_s} \tag{8}$$

2 Silanol Density

The density of hydroxyl groups is important in determining the surface charging properties of silica and IS-FET response; for example, the hydroxyl group density has been used to rationalise the increased sensitivity of HfO_2-coated IS-FETs over SiO_2-coated IS-FETs [13,14]. Depending on the precise treatment of silica, the density can vary from none (e.g. $0\,OH/nm^2$ for >1200°C heated silica in vacuum) to high (e.g. $9.4\,OH/nm^2$ quartz surface [15]), however a fully hydroxylated surface is known to have a physiochemical constant value of between 4–6 OH/nm^{-2}, with a mean at around $4.9\,OH/nm^2$ [16,17]. Hydration of a heat-treated silica sample will eventually result in hydroxylation and convergence upon this physio-chemical constant density, although the time required varies depending on the pre-treatment of the silica sample; samples pre-treated up to 400°C in vacuum rehydroxylate readily in water at room temperature, whilst a fully dehydroxylated sample could take years at room temperature or hours in boiling water [17]. Based on this evidence, the density of $4.9\,OH/nm^2$ might be expected for the silica-surface of IS-FETs sensors which have been hydrated for sufficiently long or prepared via wet thermal oxidation, and those which have been prepared by dry thermal oxidisation and recently hydrated surfaces are expected to show a highly preparation-dependent density, which is less than $4.9\,OH/nm^2$.

3 Molecular Model Structure and Setup

3.1 Silica Model Setup

In this work, the crystalline silica model from the INTERFACE silica database was used [15]. This model consists of a Q^3 isolated silanol terminated surface, derived from the $(10\bar{1})$ cleavage plane of α-cristobalite, with a surface area of 33.4076 Å x 34.8705 Å and a slab thickness of ∼25 Å. The model is shown in Figure 1(a) of the main text and the surface shown in Figure 1(a) in this Supplementary Information. The model has a silanol density of 4.804 OH nm^{-2} in its fully protonated state. This density is most typical of small (< 200 nm) silica nanoparticles, silica glasses and porous silica, according to the literature review of Emami et al. [15]. The silanol density of ∼5 OH nm^{-2} has been used by other authors to successfully reproduce experimental IS-FET data [18], is often used in IS-FET modelling [19] and is expected to be the density of fully hydrated silica as discussed in Supplementary Information 2. The system was prepared as follows: firstly, atoms were shifted 2 Å up in the z direction in order to remove contacts with the periodic boundaries. Secondly, silanolate groups on the base of the cell were protonated to form a fully hydroxylated side of the slab.

An amorphous silica model was also considered based on the model provided in the INTERFACE model database [15]. This initial atomic arrangement originated from that supplied with the Material Studio software, which is reported to have been constructed using the procedure of Vyas et al. [20]. The model consists of a 40.3148 Å x 41.4320 Å with a thickness of ∼23 Å and is shown in Figure 1(b) of the main text and the surface in Figure 2(b) in this Supplementary Information 1. For both models, atoms within ∼11 Å of the base were rigidly constrained for all simulations to emulate a silica bulk.

The surface area was calculated using the Material Studio 'Atoms, Volumes and Surfaces' tool for the final frame (i.e. after 360 ns molecular dynamics) of the uncharged crystalline and amorphous silica models. The surface area of both the top and bottom of the slab was combined, using a mesh resolution of 0.4 Å, Van der Waals scale factor of 1 Å, a maximum solvent radius of 2 Å and a solvent probe radius of 1.4 Å. The resulting solvent accessible surface area was 2995.23 $Å^2$ and 4593.32 $Å^2$ for the crystalline and amorphous models respectively, i.e. a 53% larger surface area for the amorphous system. Images of the surface of the crystalline and amorphous systems are shown in Figure 1.

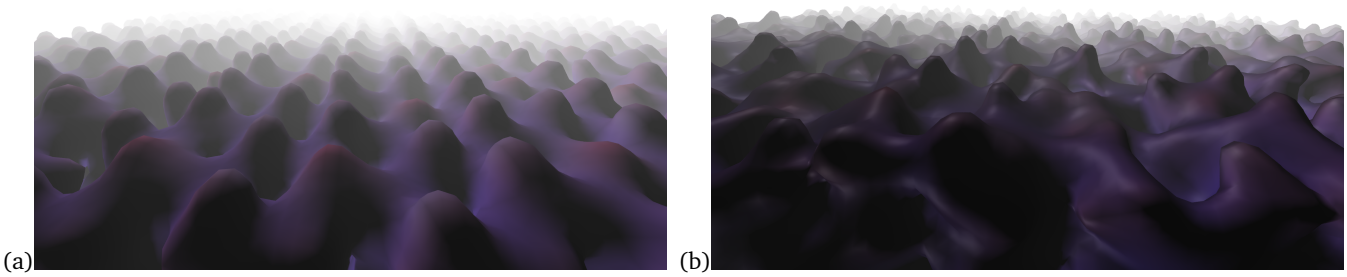

Figure 1 Surface representation of the $-0.16\,Cm^{-2}$ surface charge density silica systems after the equilibration period in liquid. (a) Crystalline system, (b) amorphous system. Images generated using VMD v1.9.3 'QuickSurf' with probe radius scale of 0.8 Å, density isovalue of 1.7, resolution 1.0 and grid spacing 0.6 and the Tachyon software for rendering shadows.

3.2 Liquid-phase Setup

The solvent box was initialised within 1 Å of the surface. A TIP3P solvent box was generated commensurate with the silica unit cell, and a thickness of 73 Å. Ions in the bulk solvent box (sodium and chlorine) were placed randomly. Both water and ions were generated using Visual Molecular Dynamics (VMD) software's 'solvate v1.7' and 'autoionize v1.3' plugin respectively. 300 mM of NaCl was added, with the specific number of ions added based on the dimension of water box. Chloride ions were initialised randomly. At thermodynamic equilibrium, any two system duplicate systems are expected to reach a consistent density of bound counter ions regardless of initial conditions and therefore, in order to test convergence to equilibrium, two initial configurations of the Na^+ were considered. In one configuration, the neutralising Na^+ was initialised close to the surface, and in the other, they were initialised randomly distributed in the solvent region. A 265 Å z-dimension for the unit cell was used [21] unless otherwise specified, which results in a generous vacuum space of approximately 165 Å to minimise undesirable periodic interactions between the top and bottom of the cell. A control simulation at low ionic strength was also considered (Supplementary Information 4).

3.3 DNA Setup: Main Text

The initial canonical DNA dodecamer (5'-GGGGGGGGGGGG-3') structure was constructed using the popular make-na server by J. Stroud (2010, http://structure.usc.edu/make-na/server.html, accessed October 2017) and parameterised using the CHARMM36 force-field. To ensure sufficient solvation between the DNA and the air-water interface, a water box larger than than the water box for the simulations without DNA was used. The water box height was 100 Å (with a cell z-dimension of 287 Å, vacuum spacing of approximately 165 Å). Similarly to the bare silica-electrolyte systems, two repeats were performed with different initial electrolyte configurations.

One with random initial configuration of ions and one with ions placed close to the charged surface. In the latter case, the 'cionize' plugin of the VMD software was used to initially place ions based on electrostatically favourable locations around the DNA and surface. The atomic content and unit cell details are for the simulation is summarised in Table 1.

As discussed in the main text, the DNA was initially harmonically constrained such that it remained close to the surface. In an experimental system, usually chemical functionalisation would be used to constrain the DNA but herein harmonic constrains are used for simplicity, as the aim is to provide a proof-of-concept rather than an analysis of DNA-surface interactions. 320 ns equilibration was performed followed by 180 ns both with harmonic constraints ($1\,\mathrm{kcal\,mol^{-1}\,\AA^{-2}}$) applied to DNA atoms and then 180 ns with no constraints applied. 1 ps timestep was used for all DNA calculations.

In order to test temporal convergence, the constrained DNA models were extended for 180 ns and the potentials and electric fields re-calculated over this new 180 ns period in the same manner. The calculated potential and electric field did not change significantly, suggesting that the systems had stabilised. The results presented in the main text are from this final 180 ns (i.e. 680 ns total simulation time per constrained DNA simulation).

Model	$\rho\,(\mathrm{pH_{eff}})$	SiO^-	Cl^-	Na^+
Crystalline $4.81\,\mathrm{OH/nm^2}$ $33.5\,\text{Å}\times34.9\,\text{Å}\times100\,\text{Å}$ thickness 300 mM Water box + DNA (-24 q)	-0.0825 (~6.4)	6	21	24+21+6

Table 1 Simulated System details for the DNA simulations in the main text. Model properties such as dimension and silanol density are shown in the first column, with other columns indicating the surface charge density (ρ) in units of $\mathrm{Cm^{-2}}$ and number of silanolate, chloride and sodium ions respectively.

3.4 DNA Setup: Repeat Using Different B-DNA Dodecamer

In addition to that described in the main text, a dodecamer B-DNA molecular structure obtained from solution Nuclear Magnetic Resonance (NMR) measurements (RCSB PDB ID: 103D) [22], with sequence 5'-GTGGAATGGAAC-3', was investigated. The same solvation box as the 300 mM crystalline simulation was used (73 Å thickness, but with additional sodium ions to neutralise the DNA charge). A similar shift in electric field and potential was found as shown in Figure 2, providing further evidence of the reproducibility of the simulated response due to DNA shown in the main text. This result was not included in the main text as two of the terminal groups of the phosphate were incorrectly atom typed/parameterised, to be less negatively charged than they should be based on the CHARMM36 forcefield.

Computational Methods: For this simulation, 270 ns NPT dynamics of rigid constrained DNA with 300 mM NaCl bulk solution was performed to provide an initial configuration of ions around the DNA, then the DNA, with this initial configuration of ions, was placed normal to the silica surface. A further 320 ns of NVT dynamics were performed with the DNA constrained via harmonic constraints ($1\,\mathrm{kcal\,mol^{-1}\,\AA^{-2}}$) to investigate the effect of surface-bound DNA, and diminish any significant effect of biomolecule dynamics. These constraints were then removed, allowing free diffusion of the DNA for a further 320 ns of NVT dynamics. Similarly to the simulations without DNA, electrostatic properties were calculated by analysing the last 180 ns.

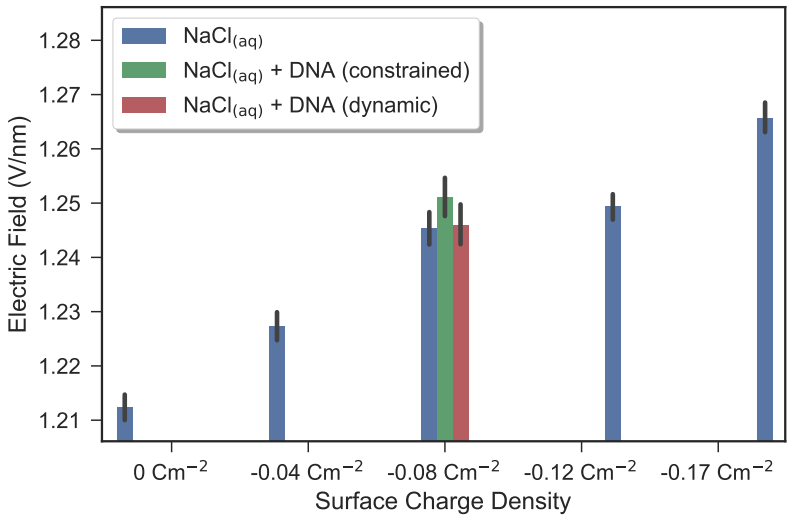

Figure 2 Bar chart of the electric field as a function of surface charge density for the crystalline silica model for a different DNA sequence than the one used in the main text. The electric field is calculated from the force on a test charge below the silica substrate similarly to that shown in the main text. The blue bars show the electrolyte-only system, where each blue bar represents the combined data from two repeat simulations. The error bars shown are the bootstrapped 95% confidence interval. The green bar and red bar show systems including DNA constrained near the surface and free to diffuse system, respectively. From the green bar, it can be seen that there is a change in electric field due to the introduction of DNA which was constrained near the surface (within 1 nm of the surface). After the constraints were removed, the DNA diffused away from the surface (lowest position of the DNA fluctuating between approximately 1–3 nm, from the surface), resulting in no significant change in the electric field compared to the control.

4 Control Simulation Setup and Results

As a control simulation, in order to investigate the effect of ionic strength, the crystalline silica model was used with the water box containing deionised (0 mM ionic strength) solution, and charge neutrality maintained by the addition of sodium ions (initialised within several angstroms of the surface). The system details are summarised in Table 2.

Model	$\rho(\mathrm{pH_{eff}})$	SiO^-	Cl^-	Na^+
Crystalline 4.81 OH/nm^2 33.5 Å×34.9 Å Deionised control	0	0	x	$0+x$
	-0.0413	3	0	3
	-0.0825	6	0	6
	0.1238	9	0	9
	-0.1650	12	0	12
	-0.3851	28	0	28

Table 2 Simulated System details for the control simulation with 0 mM ionic strength electrolyte, showing some model properties such as dimension and silanol density, with other columns indicating the surface charge density (ρ) in units of $\mathrm{Cm^{-2}}$ and number of silanolate, chloride and sodium ions respectively.

It should be noted that the low ionic strength means that a bulk is not guaranteed to be formed within the length of the simulation cell, and thus the some artefact may occur due to the periodic boundary conditions imposing relaxation of the charge fluctuations within the system[23]. Longer simulation times are also expected to be required in order to obtain good statistical averages given the reduction in ion density.

Analysis was performed in the same way as described in the main text. The cumulative charge distribution is shown in Figure 3. The cumulative sodium ion density in the Stern-like layer is very similar to the 300 mM simulation shown in the main text because all the sodium ions accumulated within 10 Å of the surface. In contrast to the 300 mM solution simulation, the sodium ion density is therefore necessarily lower in the control simulation. The water polarisation also extended much further into the bulk, as can be seen by comparing Figure 4 to the water orientation observed in the higher ionic strength simulations (Supplementary Information 8). This is indicative of the surface charge being less effectively screened by sodium ions and thus the electric field from the surface charge extends further into the bulk.

For a given surface charge there was a greater change in surface potential for the control system as compared to the 300 mM systems in the main text, as expected from mean-field models of the electrical double layer. As the empirical relation between surface charge and experimental pH used in the main text is calibrated for high ionic strength systems (0.1–0.3 M), direct comparison of the of the effective pH–surface potential response for this control simulation with the 0.3 M system of the main text is not informative.

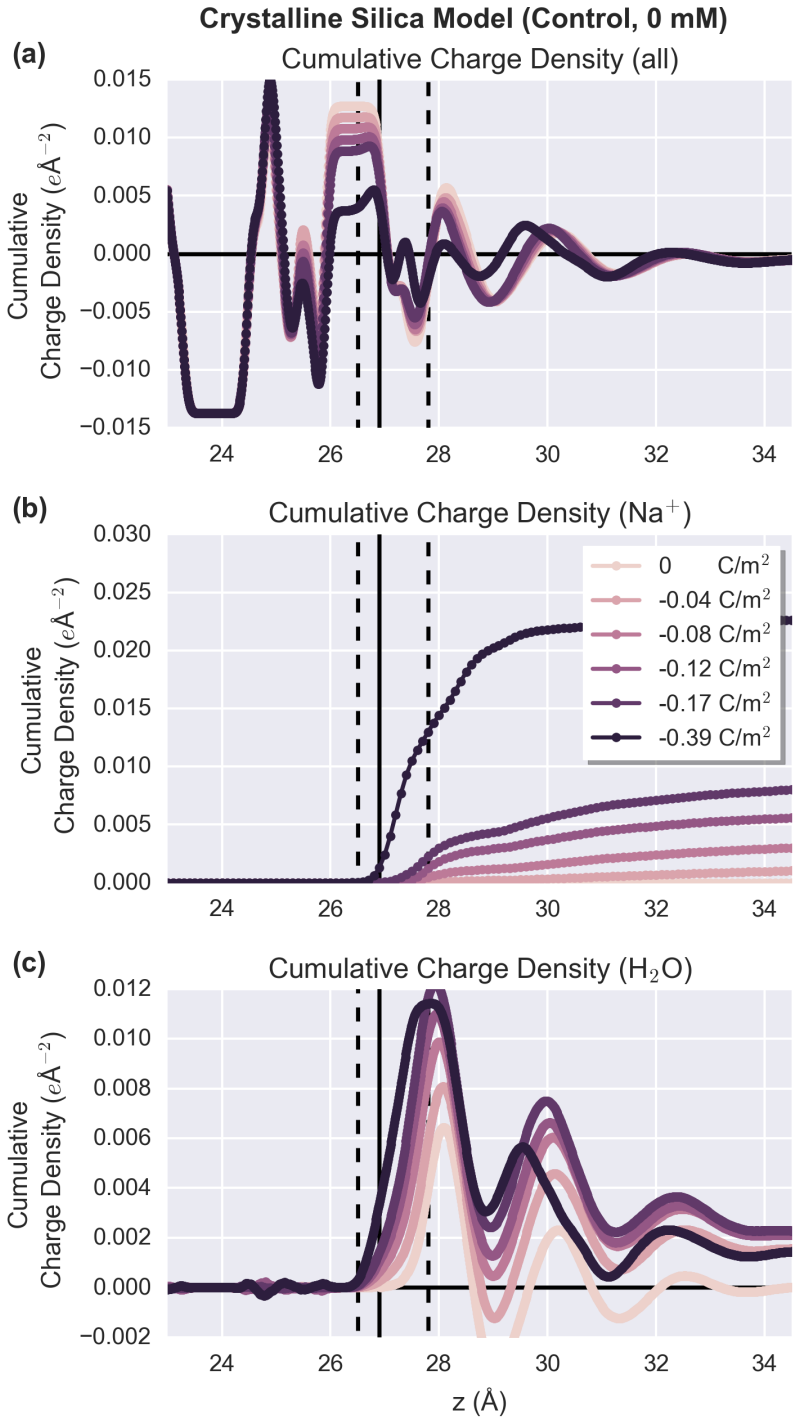

Figure 3 The integrated charge density of the system as a function of z position for increasing surface charge density (from light to dark lines) for the crystalline silica model 0 mM bulk ionic strength (a,b,c). Subfigures are shown for the combined charge density of all atoms (a), only the sodium ions (b), and only the oxygen and hydrogen atoms in water molecules (c). For each plot, the integration was performed from the silica (at $z = 0$ Å) to the bulk water. For the crystalline model, the silanol density showed two peaks, the largest at 27.0 ± 0.1 Å and a smaller peak at 27.5 ± 0.1 Å. Shown on the figure with solid black vertical lines is the surface definition described in the methods section. Dashed vertical black lines indicate the upper and lower bounds in which charged silanolate groups were present.

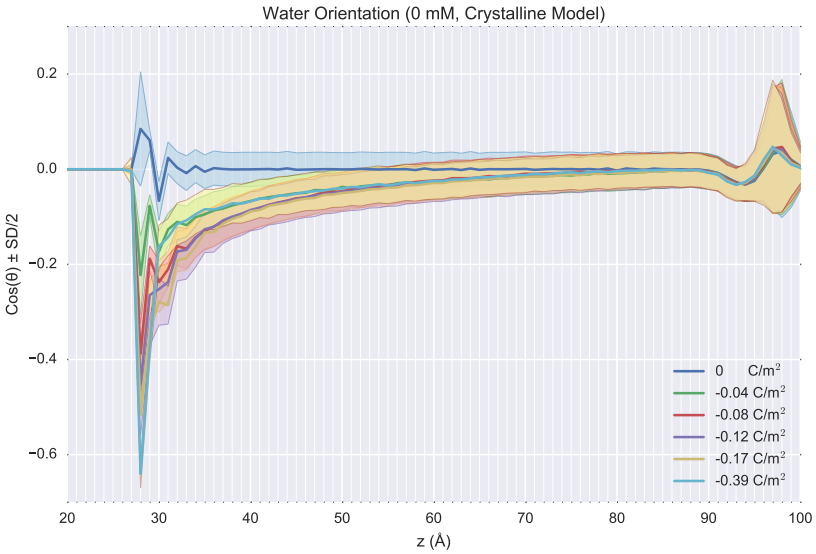

Figure 4 Orientation of water shown for the 'control' simulation in which the electrolyte contained only sodium ions to neutralise the negative charge of the surface (i.e. deionised water, or 0 mM ionic strength electrolyte), using the crystalline silica model. A value of $\cos(\theta) = -1$ corresponds to hydrogen down (towards the negatively charged silanolate groups of the surface), 0 to isotropic and 1 to hydrogen up. It can be seen that a larger unit cell is required for this system as the region of no net orientation is only reached near the top layer of the water box - this long-range ordering of water molecules is because this low ionic strength, there is little screening of the surface charge by electrolyte ions. The shaded regions show half the standard deviation above the mean, and below the mean.

5 DNA Trajectory Snapshots

Snapshots from the unconstrained and constrained DNA system from the main text are shown in Figures 5 and 6, respectively. Snapshots were taken at 10 ns intervals, and are from the simulation in which sodium ions were initialised using the 'cionise' plugin described in Supplementary Information 3.3. Snapshots are shown starting from after equilibration.

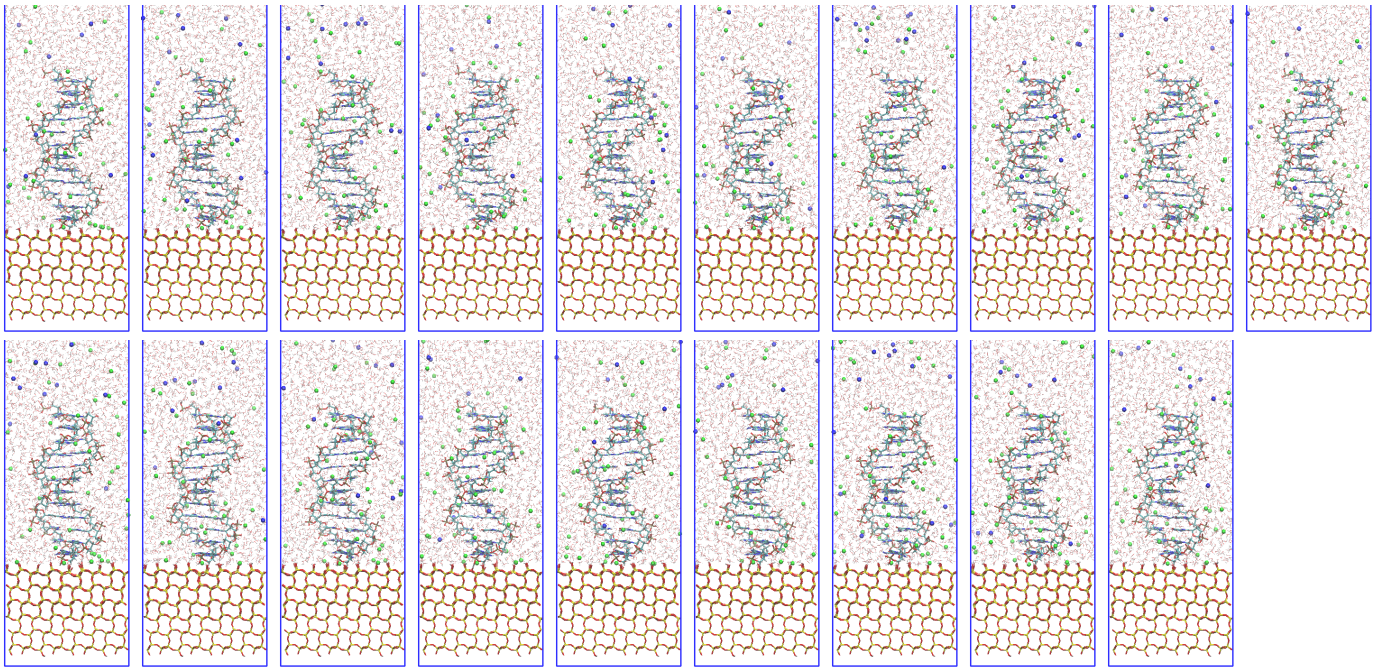

Figure 5 Time-series snapshots from one repeat of the 'constrained' DNA simulation from the main text, i.e. after equilibration, showing snapshots from the trajectory with harmonic constrains applied for 180 ns. Images are shown with the top left image at the initial time, progressing from left to right, then onto a new line from left to right, with intervals of 10 ns between each snapshot, and the final snapshot being at 179 ns in the bottom right hand side. For clarity, water molecules are shown as semi-transparent and ions are not shown. White, red and yellow corresponds to hydrogen, oxygen and silicon atoms, respectively. Each image is zoomed in on the DNA, i.e. the top of the image is not the top of the unit cell.

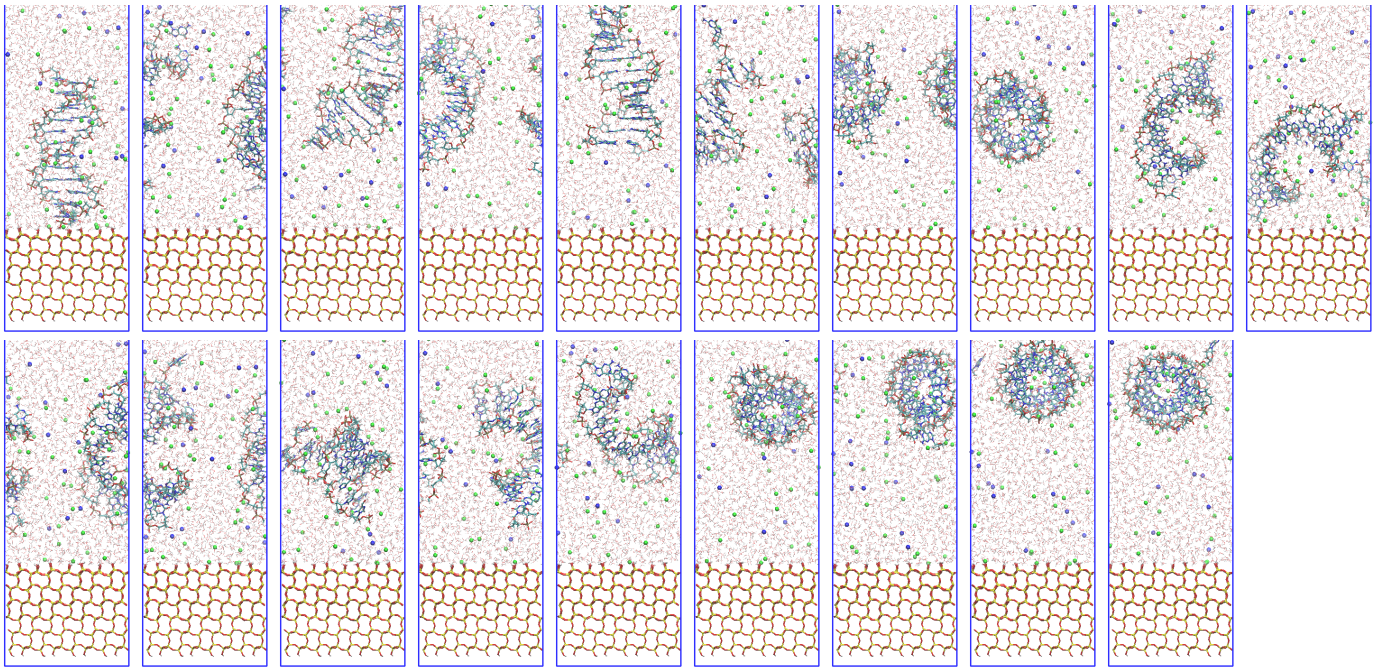

Figure 6 Time-series snapshots from one repeat of the 'unconstrained' DNA simulation from the main text. The first snapshot is at the initial point, with harmonic constraints applied, and subsequent snapshots after the DNA system is unconstrained. Images are shown with the top left image at the initial time, progressing from left to right, then onto a new line from left to right, with intervals of 10 ns between each snapshot, and the final snapshot being at 179 ns in the bottom right hand side. Within 10 ns, the DNA has diffused more than 1 nm from the surface. For clarity, water molecules are shown as semi-transparent. Green spheres, dark blue sphere, white, red and yellow corresponds to sodium, chlorine, hydrogen, oxygen and silicon atoms, respectively. DNA is drawn using stick representation, with carbon in teal and nitrogen in dark blue. Each image is zoomed in on the DNA, i.e. the top of the image is not the top of the unit cell.

6 INTERFACE Forcefield Validation

Under physiologically relevant conditions (i.e. pH ~6–9), the surface is highly charged but most silica-water forcefields do not have parameters to describe the negatively charged silanolate groups at the surface. In contrast, the INTERFACE forcefield was parameterised for hydrated silanolate groups. The INTERFACE forcefield shows excellent agreement with experiment for a large range of experimental data such as water contact angle, adsorption energy of peptides (at 20% surface ionization), water adsorption isotherms, immersion energy in water and the cell parameters of quartz[24]. The density of ions in the diffuse region of the surface (~3 Å away from surface) was calculated by Emami et al and shown to have increased density of cations with increasing surface charge density[15]. This observation is in qualitative agreement with zeta potential measurements which show an increase in zeta potential with increasing pH[25,26]. At very high surface ionisation (>26%, 0.04 C/m^2), they showed a reduction in mobile sodium ions density[15] which is not observed in experimental zeta potential measurements[25–27]. At high pH (> pH 9), however Emami et al. observed that this is in qualitative agreement with trends in the swelling of clay materials. The forcefield has also been used to simulate protein binding, showing good agreement to measured binding isotherms[28].

6.1 INTERFACE Parameters

The INTERFACE v1.5 forcefield used in this work provides CHARMM force-field compatible parameters for silica and sodium ions[24]. The INTERFACE Na model (charge=+1 e,σ_{ii} =3.17 Å, ε_{ii} =0.094 kcal/mol)[15,24,28–30] differs from the CHARMM sodium parameters (charge=+1 e, σ_{ii} =2.7275 Å, ε_{ii} =0.0469 kcal/mol)[31]. The CHARMM22 chloride (charge=−1 e,σ_{ii} = 1.1135 Å, ε_{ii} =0.150 kcal/mol) and (CHARMM27) TIP3P parameters for water were used. As the INTERFACE forcefield uses a modified Na^+ parameters, comparison of its performance to experimental data was performed for validation purposes and found reasonable agreement with experimental data, as discussed in Section 6.2.

6.2 INTERFACE Sodium Radial Distribution Function

A single Na^+ was placed in a 20 Å^3 water box and 20 ns (NPT thermostat) molecular dynamics were performed. The radial distribution function (RDF) between oxygen atoms and the sodium ion was calculated over the last 6 ns in 1 ps intervals and plotted (blue line) in Figure 7. The first maxima in the RDF was at 2.53 ± 0.1 Å which compares favourably to X-ray diffraction data reported as 2.3–2.4 Å[32] or 2.4–2.5 Å[33] and neutron scattering data reported as 2.37 Å[34]. The RDF was then integrated (green line, 7) and used to estimate the coordination number of 6.3 (indicated by black horizontal line). This slightly overestimates neutron scattering data which estimates a value of 4.9 ± 1[32] and overestimates compared to *ab initio* MD of 4.6[35].

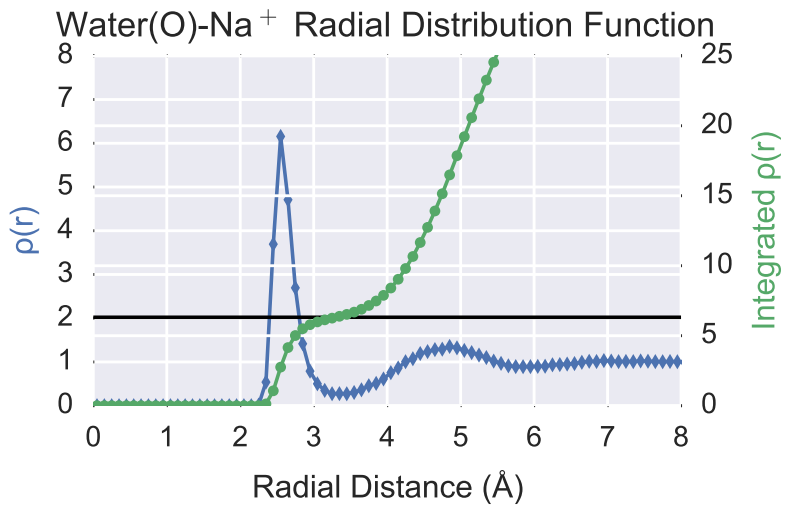

Figure 7 Radial Distribution Function (blue diamonds) between the oxygen atom of water and Na^+ in bulk water showing a first solvation shell at 2.4–2.6 Å and a secondary diffuse hydration shell at around 4–6 Å. The integrated curve (green circles) is also shown, demonstrating a simulated coordination number of 6 (black line) (i.e. hexahydrate first solvation shell)

7 Simulation Setup

The NAMD software was used in this work, which was developed by the Theoretical and Computational Biophysics Group in the Beckman Institute for Advanced Science and Technology at the University of Illinois at Urbana-Champaign[36]. The NAMD parameters were:

```
#Using NAMD 2.12 for Linux-x86_64-verbs
temperature           298.15
exclude               1-3
cutoff                12.0
switching             off
pairlistdist          14.0
timestep              2    #For DNA simulations=1
nonbondedFreq         2    #For DNA simulations=1
fullElectFrequency    2    #For DNA simulations=1
rigidBonds            all
useSettle             on
langevin              on
langevinDamping       1
langevinTemp          298.15
PME                   yes
PMEGridSpacing        1.0
PMETolerance          0.000001
```

The particle-mesh Ewald (PME) method was used for efficient electrostatics evaluation with periodic boundary conditions and the EW3DC correction implemented based on the code of Yeh et al.[37,38]. A 1 Å grid spacing and 1×10^{-6} tolerance and a local interaction distance of 12 Å was used.

7.1 Harmonic Restraints to Prevent Water Evaporation

Over the duration of each simulation (~320 ns), several water molecules were found to evaporate into the vacuum layer and cross the z-periodic boundary. This "water noise" prohibits accurate calculation of the electrostatic potential of the system[39] and therefore, similar to other literature[40], a simple repulsive potential was employed to prevent this (Equation 9). More specifically, a list of atoms which were at a z coordinate greater than that of the wall ($z_0 = 120$ Å) was generated and updated every 100 steps (200 fs), and every step a force, F, was applied to atoms in the list:

$$F = -k(z - z_0), \tag{9}$$

where k is a harmonic force constant of -1 kcal mol^{-1} Å^{-2}.

7.2 Analysis Methodology

The electric field in Figure 4 of the main text was calculated as the electric field on a test charge, as per our previous work[41], with the test charge at z =0.5 Å and at the central x and y positions, below the silica substrate. The system is non-neutral due to the test charge and forces were calculated exactly using the nearest neighbour periodic boundary conditions.

Calculation of the charge density z profile was performed using the VMD density profile tool[42]. A mesh spacing (i.e. slab $z-$thickness) of 0.01 Å was chosen for this study, which provides a surface potential converged to within 2 mV of the value calculated for the 0.001 Å mesh[21].

Analysis of the electric potential as a function of time suggested that at least 100 ns equilibration was required[21]. Simulations were performed for 320 ns, with the final 180 ns used at picosecond intervals for analysis. In order to quantify error from temporal fluctuations, the surface potential was calculated over three 60 ns windows and the standard error across these simulations was calculated. In order to further test whether thermodynamic equilibrium has been achieved, two separate simulations were run for each system with different initial conditions.

The amorphous -0.0480 Cm^{-2} model system in which the ions were initially randomly placed ("System A") showed a water distribution which was anomalously polarised and a surface potential which was anomalously negative and large in magnitude (approximately -125 mV) when compared to the repeat ("System B") which had ions placed close to the surface (as described in the methods). The results of System A were also anomalous with regard to the trend seen in water polarisation at higher and lower surface charge. This was indicative of poor convergence to thermodynamic equilibrium and so a simple annealing procedure was used. Both System A and System B were heated to 340 K for 90 ns then run for a further 180 ns at 300 K. Upon analysis of these 180 ns, System B showed no large changes in potential or water distribution, and the anomalous potential and water distribution of System A was no longer seen, with these properties similar between Systems A and B. This similarity is indicative of attaining thermodynamic equilibrium and these last 180 ns of annealed System A were used in the main text.

The bulk potential after the 180 ns equilibration period was stable over time in all simulations, showing a standard deviation of 0.6 ± 0.1 mV (SD) across all simulations and therefore not a significant source of error. For calculations in which qualitative accuracy was sufficient (water orientation calculations and water and sodium ion density calculations), a less computationally expensive sampling was used in which only the last 60 ns of the trajectory was used with frames analysed every 10 ps.

The cumulative polarisation number density of water across the Stern-like layer (Figure 3(a) from main text) was calculated by calculating the polarisation as follows: The number density of the oxygen atoms of water as a function of z was calculated using 1 Å bins. Then the polarisation was integrated from the surface to the second minima in the water density profile to obtain the cumulative polarisation number density of water across the Stern-like layer. The polarisation was defined similarly to Mandadapu et al.[43] and Lee et al.[44] as the dipole moment of TIP3P water (2.354 Debye) multiplied by the average orientation of water molecules within each bin (with respect to the z axis, $cos(\theta)$), multiplied by the number density within each respective bin.

8 Water Orientation

The orientation of water with respect to the surface normal for the crystalline system and amorphous 300 mM systems from the main text are shown in Figures 8 and 9, respectively. In all simulations, the water became increasingly oriented with hydrogen down towards the negative silanolate groups as the silanolate surface charge density was increased. Interestingly, the models with no silanolate groups showed the opposite orientation of water molecules near the surface (oxygen towards the silanol), however from the water charge density plots in the main text, it can be seen that the density of water molecules in this region (26–27 Å) is vanishingly small, so it is not significant from the perspective of understanding the dominant electrostatics. To better understand the electrostatics and account for relative density of water molecules, in the main text, the polarisation is calculated instead of the orientation.

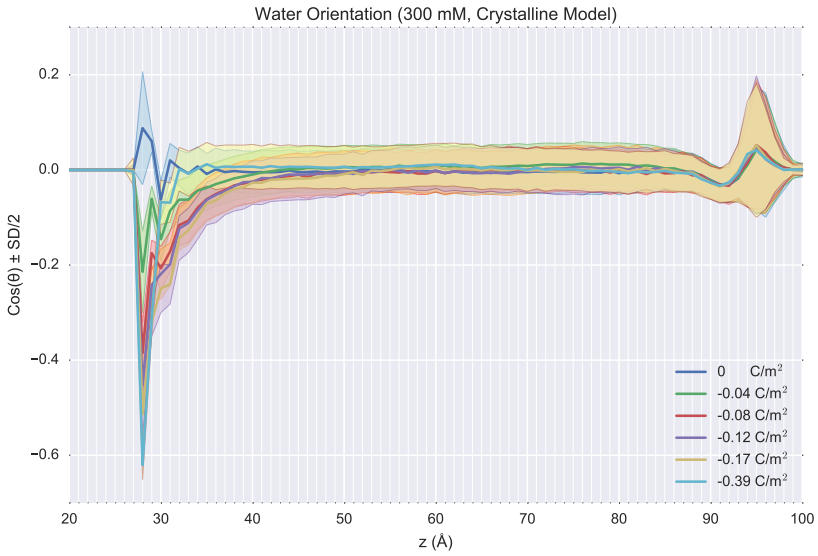

Figure 8 Orientation of water for the 300 mM NaCl using the crystalline silica model. The filled area shows the variation as half the standard deviation above and below the mean, demonstrating a reduction in variation close to the surface and an increase in surface orientation. A value of $\cos(\theta) = -1$ corresponds to hydrogen down (towards the negatively charged silanolate groups of the surface), 0 to isotropic and 1 to hydrogen up.. Only one of the two repeat simulations is shown.

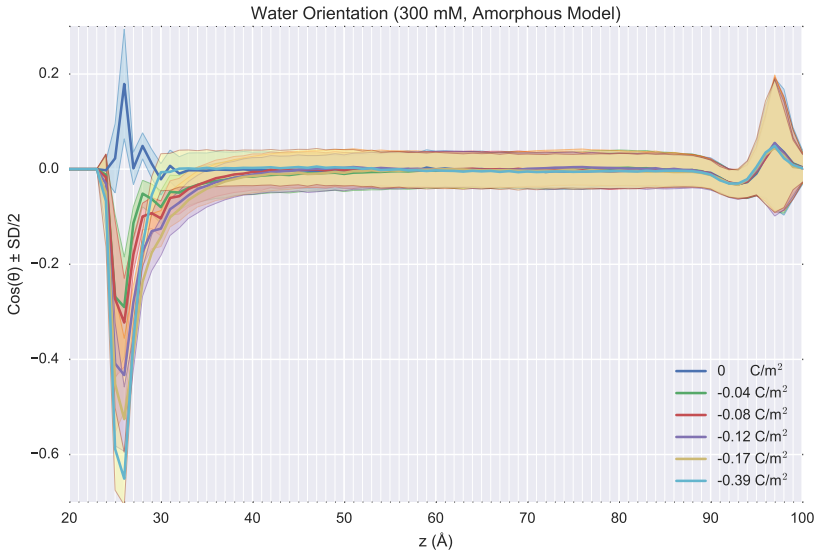

Figure 9 Orientation of water for the 300 mM NaCl using the amorphous silica model. The filled area shows the variation in water orientations across the 60 ns window, as half the standard deviation above and below the mean, demonstrating both a reduction in variation close to the surface and an increase in surface orientation . A value of $\cos(\theta) = -1$ corresponds to hydrogen down (towards the negatively charged silanolate groups of the surface), 0 to isotropic and 1 to hydrogen up. Only one of the two repeat simulations is shown.

9 Correlation between Electric field and Total Electrostatic Energy

As discussed in the main text, a correlation was identified between the electric field below the substrate and the total electrostatic energy of the system calculated by double integration of the charge density as in the main text.

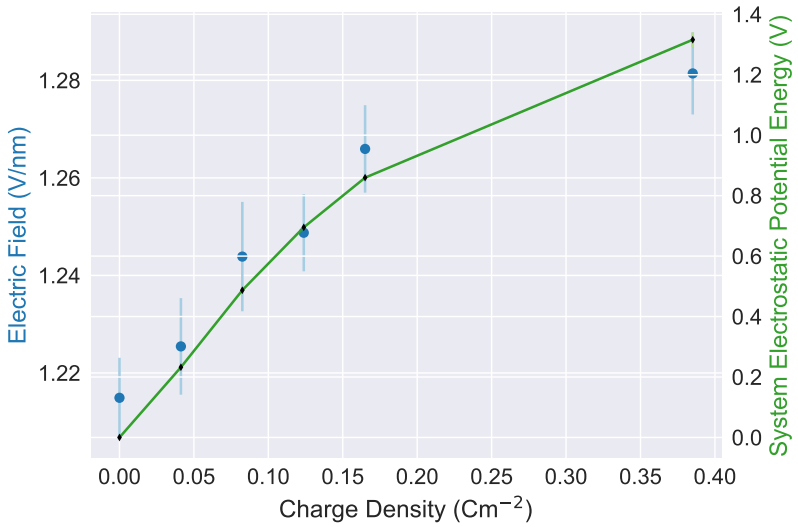

Figure 10 Electrostatic potential stored in the system (black markers and green solid line), and the z-component of the electric field (blue circles) on a test charge below the amorphous silica model substrate, plotted as a function of negative silica surface charge density. The figure shows the long-range influence of the interfacial electric field below the silica. Increasing surface charge resulting in a linear increase in electric field for surface charge densities $\leq 0.165\,\mathrm{C/m^{-2}}$, followed by a sub-linear increase at extremely high surface charge densities. The electrostatic potential calculation was calculated from the base of the system (vacuum potential at $z = 0$ Å) to the bulk water (mean potential between $z = 60 - 70$ Å). The electric field was calculated as the electrostatic force on a positive test charge 3 Å below the silica substrate, located at the central point of the x,y plane, using a Coulombic sum over the unit cell and its nearest neighbours in all three dimensions.

10 Effect of Simulation Duration

With increased duration of molecular dynamics simulation there are two benefits: firstly, the molecular dynamics simulations sample more conformational space and are more likely to reach thermodynamic equilibrium, and secondly if the property is noisy on short time scales, then by averaging over longer times scales more precise estimates of the mean can be obtained (smaller standard error of the mean). In this section, we demonstrate the benefits of the extended simulation duration performed for this work compared to similar literature.

At least 90 ns was found to be required for convergence of the potential to within millivolt stability, this is shown in Figure 11.

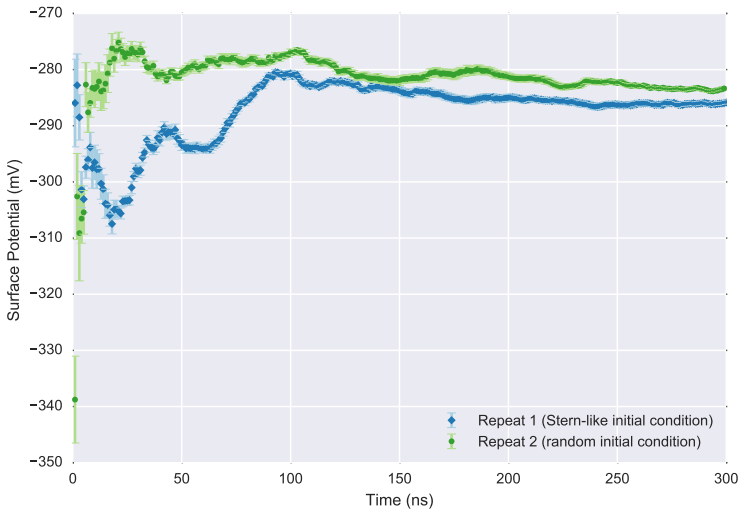

Figure 11 The mean surface potential from $t = 0$ to t ns is shown for the 300 mM NaCl crystalline silica simulation with surface charge density $-0.0413\,\mathrm{Cm}^{-2}$, with two different initial configuration of NaCl ions, one in which the negative surface charge is initially compensated by sodium ions within several angstroms, and the remaining electrolyte ions are randomly distributed (shown in blue) and another in which all ions were initially randomly distributed (green). $t = 0$ represents the initial structure after energy minimisation (i.e. no equilibration period).

The ionic atmosphere around DNA is reported to require at least 300 ns[45] and therefore we ensured DNA systems were equilibrated for 320 ns.

In Figure 12, the effect of thermodynamic convergence can be seen by comparing the potential profile for an example system with 1 ns equilibration period (dashed green line) compared to a 180 ns equilibration period (solid green line). For both these calculations, the plotted potential was calculated from the mean charge density taken over 19 ns; these durations were chosen in analogy with the potential calculations of Yeh and Wallqvist[38], in which they also calculated the potential and the silica-water interface using the EW3DC correction for 19 ns after 1 ns equilibration. In Figure 12 it can be seen that 180 ns equilibration (green solid line) provides a much more stable potential across the majority of the NaCl phase, in the region from 40 Å to 80 Å, as compared to the 1 ns equilibration result (dashed green line). The resulting potential was also much closer to the accurate mean calculated over an extensive 180 ns equilibration and a 180 ns production mean (darkest purple solid line). This result can help guide suitable durations for further studies of the potential properties of the silica-electrolyte interface.

Figure 12 also highlights the importance of long durations for precise calculation of the potential, as shown by comparing the potentials between each of the solid lines, which are all shown after 180 ns equilibration (i.e. after thermodynamic convergence). The solid lines show increasing duration used in calculation of the mean, and progressively produce smoother lines closer to the stable bulk mean expected. There are large magnitude fluctuations in electric field and potential on 1 ps timescales and so the mean must be calculated over long durations for stable potential calculations within millivolt precision.

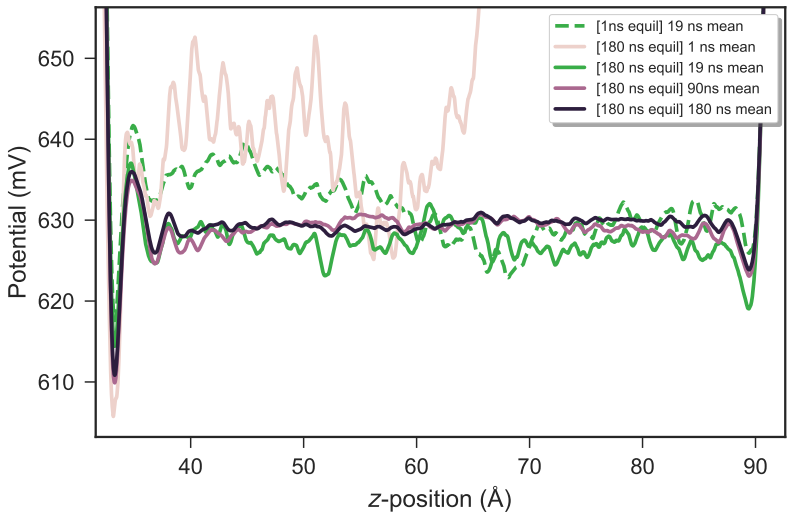

Figure 12 The mean surface potential z-distribution is shown for the 300 mM NaCl crystalline silica simulation with surface charge density $-0.1650\,\mathrm{Cm}^{-2}$ over various durations. To show the effect of thermodynamic equilibration, the dashed green line shows the 19 ns mean taken after only 1 ns of equilibration, which can be compared with the solid green line showing the 19 ns mean taken after 180 ns equilibration. Various solid lines are all shown are 180 ns equilibration, with various duration used for the mean calculation, as indicated in the legend. These solid lines illustrate how longer durations (e.g. > 19 ns) used for the calculation of the mean enable a bulk potential which is smooth and stable within the millivolt range. The absolute potential is shown (i.e. 0 V at $z = 0$, with no normalisation applied relative to other simulations or the surface/bulk potential).

The following data was taken from the end of each simulation (i.e. *after* at least 180 ns equilibration) and further highlights the role of duration in providing precise averages. The following figures compare the results of electric field (Figure 13) and surface potential (Figure 14) calculations if only a single repeat was performed for 3 ns instead of the 180 ns production average used in this work. Error bars are taken as the standard error three 1 ns segments. The 3 ns results are shown on the left hand of each figure, with the right hand side being the 180 ns result already shown in the main text.

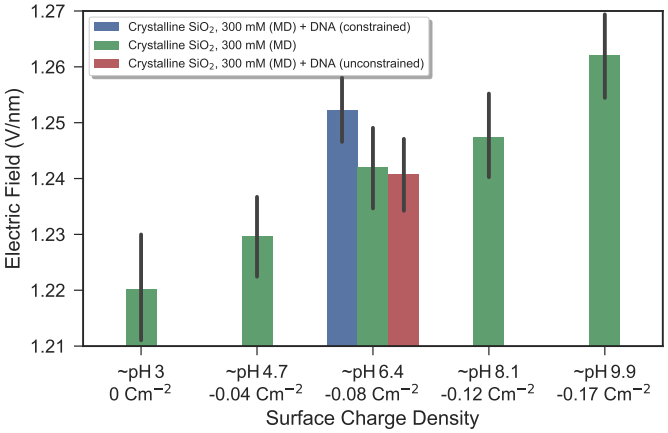

(a)

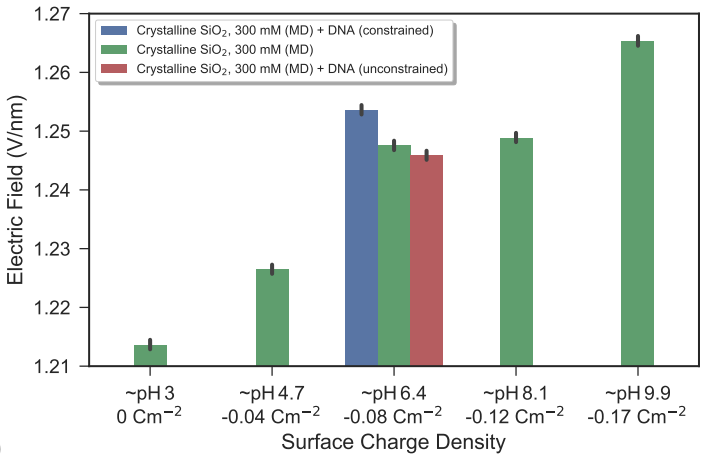

(b)

Figure 13 The importance of long molecular dynamics trajectories is highlighted by comparing the electric field for the crystalline system (and DNA) if it were calculated over only 3 ns (a) as opposed to that shown in the main text Figure 4, reproduced in (b). See the main text for detailed explanation of the figure. The figures were calculated using snapshots every 100 ps, with error bars showing 95% confidence intervals from the standard error of the mean.

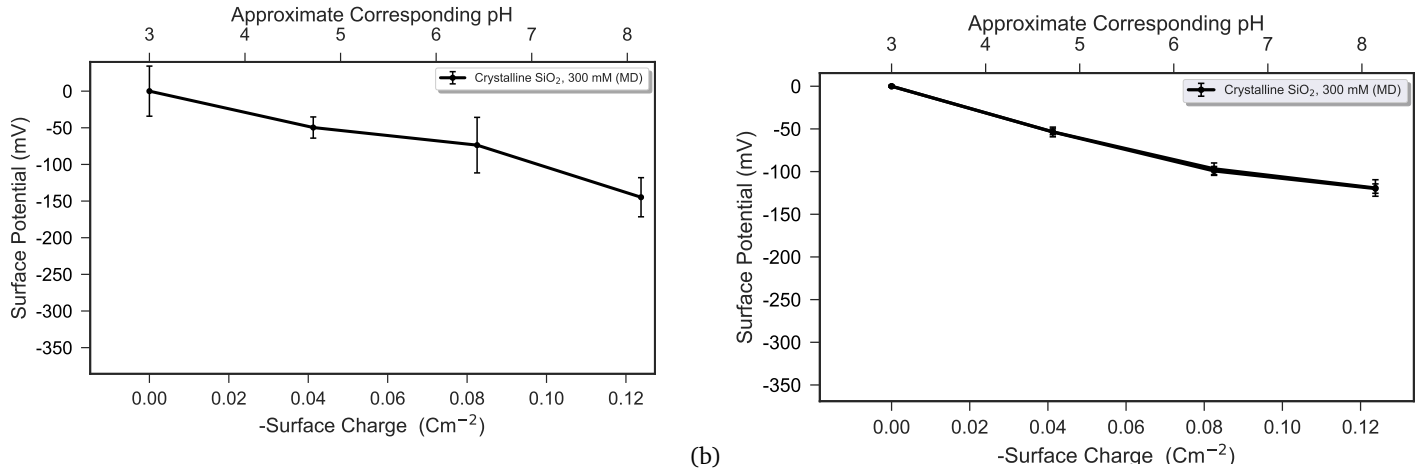

Figure 14 The importance of long molecular dynamics trajectories is highlighted by comparing the surface potential for the crystalline system if it were calculated over only 3 ns (a) as opposed to that shown in the main text Figure 6, reproduced in (b). (a) was calculated using the mean charge density for three 1 ns intervals, with error bars showing 95% confidence intervals from the standard error of the mean (n=3).

References

[1] J. O. Bockris, A. K. Reddy and M. E. Gamboa-Aldeco, *Modern Electrochemistry 2A*, Kluwer Academic Publishers, Boston, 2002, vol. 2A.

[2] X. Duan, Y. Li, N. K. Rajan, D. A. Routenberg, Y. Modis and M. A. Reed, *Nat. Nano.*, 2012, **7**, 401–407.

[3] X. Wen, S. Gupta, Y. Wang, T. R. N. Iii, S. C. Lee and W. Lu, *Appl. Phys. Lett.*, 2011, **99**, 043701.

[4] T. Sakata and R. Fukuda, *Anal. Chem.*, 2013, **85**, 5796–5800.

[5] G. Shalev, Y. Rosenwaks and I. Levy, *Biosens. Bioelectron.*, 2012, **31**, 510–515.

[6] R. J. Hunter, *Foundations of Colloid Science*, Oxford University Press, Oxford, UK, 2001.

[7] J. Lyklema, *Fundamentals of Interface and Colloid Science: Solid-Liquid Interfaces*, Academic Press, Cambridge, Massachusetts, 1995.

[8] H. Ohshima, *Biophysical Chemistry of Biointerfaces*, John Wiley & Sons, 2011.

[9] D. Grahame, *Chem. Rev.*, 1947, **41**, 441–501.

[10] J. O. Bockris and A. K. Reddy, *Modern Electrochemistry 1*, Kluwer Academic Publishers, Boston, 1998, vol. 1.

[11] M. S. Kilic, M. Z. Bazant and A. Ajdari, *Phys. Rev. E*, 2007, **75**, 021502.

[12] M. S. Kilic, M. Z. Bazant and A. Ajdari, *Phys. Rev. E*, 2007, **75**, 021503.

[13] T. Akiyama, Y. Ujihira, Y. Okabe, T. Sugano and E. Niki, *IEEE Trans. Electron Devices*, 1982, **29**, 1936–1941.

[14] S. Chen, J. G. Bomer, E. T. Carlen and A. van den Berg, *Nano Lett.*, 2011, **11**, 2334–2341.

[15] F. S. Emami, V. Puddu, R. J. Berry, V. Varshney, S. V. Patwardhan, C. C. Perry and H. Heinz, *Chem. Mater.*, 2014, **26**, 2647–2658.

[16] L. T. Zhuravlev, *Langmuir*, 1987, **3**, 316–318.

[17] L. Zhuravlev, *Colloids Surf. A Physicochem. Eng. Asp.*, 2000, **173**, 1–38.

[18] A. Bandiziol, P. Palestri, F. Pittino, D. Esseni and L. Selmi, *IEEE Trans. Electron Devices*, 2015, **62**, 3379–3386.

[19] R. E. G. van Hal, J. C. T. Eijkel and P. Bergveld, *Adv. Colloid Interface.*, 1996, **69**, 31–62.

[20] S. Vyas, J. E. Dickinson and E. Armstrong-Poston, *Mol. Simul.*, 2006, **32**, 135–143.

[21] B. M. Lowe, C.-K. Skylaris, N. G. Green, Y. Shibuta and T. Sakata, *Jpn. J. Appl. Phys.*, 2018, **57**, 04FM02.

[22] S.-H. Chou, L. Zhu and B. R. Reid, *J. Mol. Biol.*, 1994, **244**, 259–268.

[23] C. Pan, S. Yi and Z. Hu, *Phys. Chem. Chem. Phys.*, 2017, **19**, 4861–4876.

[24] H. Heinz, T.-J. Lin, R. Kishore Mishra and F. S. Emami, *Langmuir*, 2013, **29**, 1754–1765.

[25] L. Bousse, S. Mostarshed, B. Van Der Shoot, N. F. de Rooij, P. Gimmel and W. Göpel, *J. Colloid Interf. Sci.*, 1991, **147**, 22–32.

[26] P. J. Scales, F. Grieser, T. W. Healy, L. R. White and D. Y. C. Chan, *Langmuir*, 1992, **8**, 965–974.

[27] J. A. A. Júnior and J. B. Baldo, *New J. Glass Ceram.*, 2014, **4**, 29.

[28] F. S. Emami, V. Puddu, R. J. Berry, V. Varshney, S. V. Patwardhan, C. C. Perry and H. Heinz, *Chem. Mater.*, 2014, **26**, 5725–5734.

[29] F. S. Emami, V. Puddu, R. J. Berry, V. Varshney, S. V. Patwardhan, C. C. Perry and H. Heinz, *Chem. Mater.*, 2016, **28**, 406–407.

[30] S. V. Patwardhan, F. S. Emami, R. J. Berry, S. E. Jones, R. R. Naik, O. Deschaume, H. Heinz and C. C. Perry, *J. Am. Chem. Soc.*, 2012, **134**, 6244–6256.

[31] D. Beglov and B. Roux, *J. Chem. Phys.*, 1994, **100**, 9050–9063.

[32] N. T. Skipper and G. W. Neilson, *J. Phys.: Condens. Matter*, 1989, **1**, 4141.

[33] H. Ohtaki and T. Radnai, *Chem. Rev.*, 1993, **93**, 1157–1204.

[34] S. Bouazizi, F. Hammami, S. Nasr and M.-C. Bellissent-Funel, *J. Mol. Struct.*, 2008, **892**, 47–52.

[35] S. B. Rempe and L. R. Pratt, *Fluid Phase Equilibr.*, 2001, **183–184**, 121–132.

[36] J. C. Phillips, R. Braun, W. Wang, J. Gumbart, E. Tajkhorshid, E. Villa, C. Chipot, R. D. Skeel, L. Kalé and K. Schulten, *J. Comput. Chem.*, 2005, **26**, 1781–1802.

[37] I.-C. Yeh and M. L. Berkowitz, *J. Chem. Phys.*, 1999, **111**, 3155–3162.

[38] I.-C. Yeh and A. Wallqvist, *J. Chem. Phys.*, 2011, **134**, 055109.

[39] A. A. Gurtovenko and I. Vattulainen, *J. Chem. Phys.*, 2009, **130**, 215107.

[40] S. Tyagi, A. Arnold and C. Holm, *J. Chem. Phys.*, 2008, **129**, 204102.

[41] B. M. Lowe, Y. Maekawa, Y. Shibuta, T. Sakata, C.-K. Skylaris and N. G. Green, *Phys. Chem. Chem. Phys.*, 2017, **19**, 2687.

[42] T. Giorgino, *Comput. Phys. J.*, 2014, **185**, 317–322.

[43] K. K. Mandadapu, J. A. Templeton and J. W. Lee, *J. Chem. Phys.*, 2013, **139**, 054115.

[44] J. W. Lee, A. Mani and J. A. Templeton, *Langmuir*, 2015, **31**, 7496–7502.

[45] R. Lavery, J. H. Maddocks, M. Pasi and K. Zakrzewska, *Nucleic Acids Res.*, 2014, **42**, 8138–8149.